



# Outdoor measurements of relationship between canopy flow and wall pressure distributions of a block within urban-like block array

C. Hirose<sup>a,\*</sup>, N. Ikegaya<sup>b</sup>, A. Hagishima<sup>b</sup>

<sup>a</sup> Interdisciplinary Graduate School of Engineering Sciences, Kyushu University, Japan

<sup>b</sup> Faculty of Engineering Sciences, Kyushu University, Japan

## ARTICLE INFO

### Keywords:

Comprehensive outdoor scale model experiment  
Natural ventilation  
Wind pressure coefficient  
Urban boundary-layer flow

## ABSTRACT

Research on indoor ventilation is mainly conducted utilizing wind-tunnel experiments and computational fluid dynamics simulations under controlled flow conditions. However, with these techniques, the effects of the actual urban boundary-layer flow with variable wind directions and turbulence on the ventilation performance of a building surrounded by various buildings remain unresolved. Therefore, we conducted outdoor experiments at the Comprehensive Outdoor Scale Model experiment site to evaluate the mutual relationships between wall pressure of a building within a square array, in which cubical blocks are aligned in same spanwise position in a row, and atmospheric urban boundary-layer flow. The dataset consisting of the simultaneous measurements of the wall pressure acting on a target block and the air flow around it was analyzed statistically. The results demonstrate that the distributions of wind pressure coefficient significantly change with the approaching wind direction, while similar cavity flow patterns such as the downward flow at windward wall and the upward flow at leeward wall are observed regardless of the wind direction. Additionally, the pressure coefficient is more sensitive to the approaching wind direction at the side-edge than at the center of the block surface. Moreover, the temporal and spatial distributions of wall pressure are highly correlated with the fluctuating flow above the canopy rather than the turbulence generated within the canopy.

## 1. Introduction

In recent years, energy saving of buildings has become an urgent issue, especially in tropical countries with rapid urbanization and economic growth where the energy demand for space cooling to provide comfortable indoor environments has considerably increased. The utilization of natural ventilation in urban buildings has been recognized as a cost-effective solution to achieve healthy and comfortable indoor environments since stagnating indoor air is replaced with fresh and cooler outdoor air.

Natural ventilation is driven by both the buoyancy and wall pressure differences acting on the building walls and is strongly related to the flow conditions of interior and outdoor spaces. Therefore, variations in the surrounding wind environment (e.g., wind speed, direction and turbulence), geometry conditions (e.g., arrangement of neighboring buildings) and building designs (e.g., the configuration of the building, the area and shapes of the openings) make it difficult to estimate the ventilation rate accurately. For wind-induced natural ventilation, the ventilation rate,  $Q$  [ $\text{m}^3/\text{s}$ ], is calculated by Eqs. (1)–(1), based on

Bernoulli's principle for the steady incompressible flow.

$$Q = \alpha A \sqrt{(2\Delta p / \rho)}. \quad (1-1)$$

Here,  $\alpha A$  denotes the effective opening area,  $\rho$  [ $\text{kg}/\text{m}^3$ ] is the air density and  $\Delta p$  [Pa] is the pressure difference between the windward and leeward walls, which is estimated by the wind pressure coefficient,  $C_p$ . Because  $\Delta p$  acting on the target building is the driving force of the wind-induced natural ventilation, the locations for ventilation passages in a building are determined based on the distribution of  $C_p$ . However, the practical determination of  $C_p$  is highly dependent on idealized conditions such as the steady state flow, simplified building shapes and isolated configurations. Therefore, the determination of wind-induced natural ventilation under realistic conditions remains an active area of research. Previous studies on wind-induced natural ventilation have utilized the following three methods: wind-tunnel experiments (WTEs), computational fluid dynamics (CFD) simulations, and outdoor measurements.

To investigate the distribution of  $\Delta p$  acting on buildings, WTEs were

\* Corresponding author. Kasuga-koen 6-1, Kasuga-shi, Fukuoka, 816-8580, Japan.

E-mail address: [chiyoko\\_ikgy@kyudai.jp](mailto:chiyoko_ikgy@kyudai.jp) (C. Hirose).

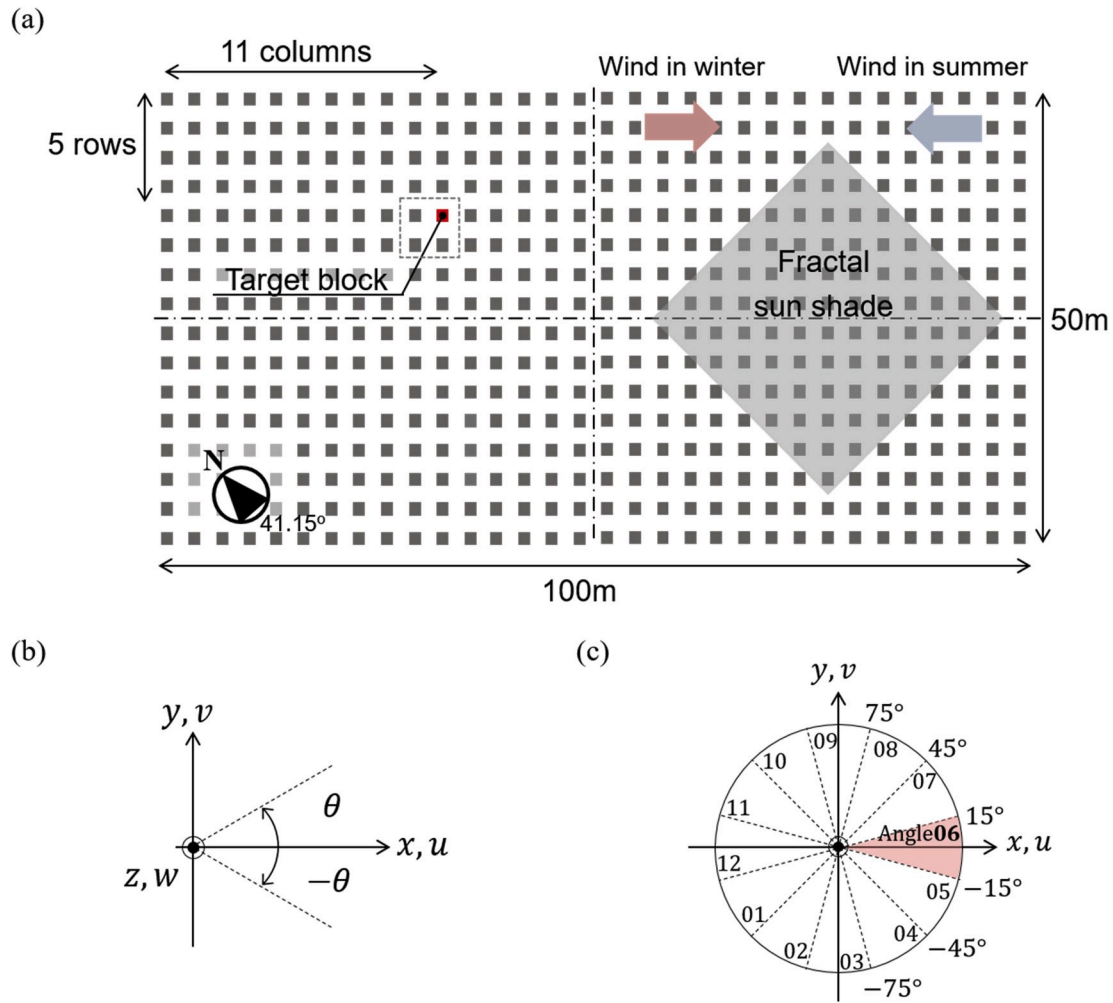


**Fig. 1.** (a) Schematic view of the comprehensive outdoor scale model (COSMO) site with prevailing wind directions, (b) definition of the wind angle,  $\theta$ , and (c) definitions of Angle 01 to Angle 12. The target block (illustrated as a red cube) is located at 11 columns and 5 rows from northern corner of the site. (For interpretation of the references to color in this figure legend, the reader is referred to the Web version of this article.)

conducted under various conditions for a variety of configurations (arrangements and shapes) of the building and ventilation openings. The initial emphasis was directed at the characteristics of wall pressure distributions and ventilation rates between the sheltered and unsheltered (isolated) cases [1,2]. Furthermore, the considerable impact of the approaching flow conditions such as the wind direction on the ventilation efficiency were highlighted by several WTE studies [3,4], emphasizing the mutual interactions between the wall pressure and the surrounding flow fields depending on the geometric condition.

CFD simulations were applied to examine the complexity as well as the non-uniformity of the flow field around and inside buildings in ventilation studies. Although the Reynolds-averaged Navier Stokes (RANS) simulations could capture only the time-averaged distributions in flow and pressure fields, they have been widely used for assessing building ventilation and environmental performances [5]. Resulting from numerous sensitivity studies of modeling constant, computing grid, and domain-size on coupled simulations of indoor and outdoor flows [6, 7], they were considered to estimate the indoor airflow and ventilation rate with acceptable accuracy. On the other hand, owing to the weakness of RANS model in reproducing the flow separation over roofs and in the wake region behind buildings [8,9], the limitation in employing the RANS simulations for the estimating ventilation rates has been discussed by several works [10,11]. In this context, large-eddy simulations (LES), which can reproduce the transient nature of the flow field, has become a popular method in accordance with recent increase in computational

performance. The previous research by LES evaluated temporal variation of the ventilation rates statistically [12] and demonstrated the importance of the instantaneous flow fields for accurate prediction of the ventilation rates [13,14]. Focusing on the origin of unsteady instantaneous flow in the boundary layer, one is small eddies generated by the surrounding buildings and the other is large eddies owing to the atmospheric turbulence above the urban canopy [15].

On the other hand, because of the limitations in the domain size and inflow conditions for WTE and CFD simulations, it is extremely challenging to reproduce large-scale motions as well as the turbulent nature of the boundary-layer flow (e.g., wind direction, speed and turbulent intensity). Therefore, field measurements (FM) could be a powerful method for understanding the fluctuating characteristics of realistic natural ventilation in urban canopies. For example, Lo et al. [16] conducted full-scale measurements of the cross-ventilation in a test house and observed the dynamic transition of the wind pressure on the surfaces, which obviously conflict with the assumptions of steady state in the conventional macroscopic model. In addition, sites that are systematically configured with simplified scale models have been utilized for outdoor experiments in ventilation studies to understand the universal relationship between flow and pressure fields. For example, with a view to clarifying the influence of surrounding blocks on the wind direction and ventilation rates, full-scale observations using a cubic test structure in isolated and urban array cases were undertaken by Gough et al. [17]. Moreover, Gough et al. [18] confirmed that the

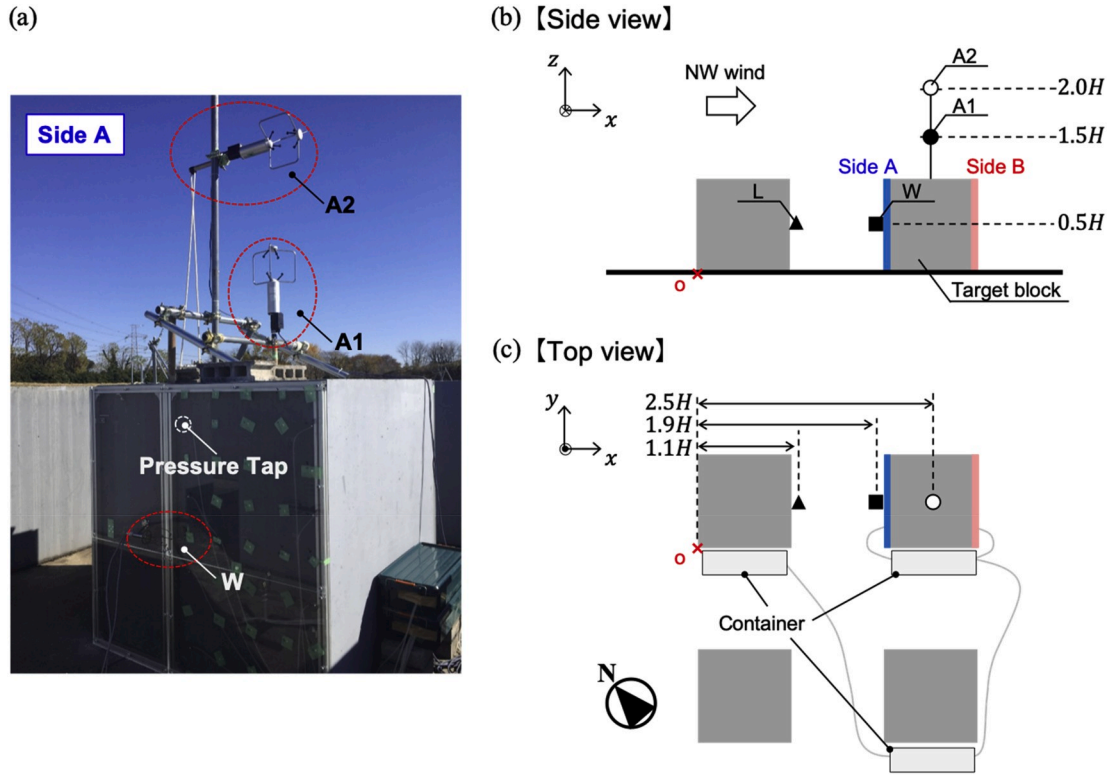


**Fig. 2.** (a) Photograph of the target block with the measurement equipment and the relative location of installed sonic anemometers to the target block, (b) schematic from southeastern side and (c) from top. The locations are defined with respect to the red cross position, “o”, and block height,  $H$ . (For interpretation of the references to color in this figure legend, the reader is referred to the Web version of this article.)

underestimations of  $C_p$  in WTEs and CFD simulations were caused by the low reproducibility of large-scale turbulence. In addition, Hirose et al. [19] conducted experiments at the comprehensive outdoor scale model (COSMO) facility and reported that the ventilation rate had significant temporal variations owing to the various scale of turbulence generated by the atmospheric flow. Although the influence of the drastic fluctuation in atmospheric turbulent flow on the surface pressure was demonstrated, studies on the natural ventilation of a building in a realistic urban boundary layer are still scarce. Specifically, simultaneous measurements of the velocity and wall pressure have scarcely been reported for a sheltered case in real urban boundary layers. Thus, data from the present study would result in the knowledge for more precise estimations of natural ventilation.

In addition, the recent works in urban climatology field have proved the turbulent organized structure (TOS) existing in roughness sublayer over urban obstacles (e.g., Kanda [20]) and its effect on the flow patterns within the canopy layer. For example, Takimoto et al. [21] has reported that the “flushing” flow, which is a significant upward motion coming from the canopy layer, is considerably related to the TOS of low-speed streak passing over the canopies. According to such knowledge about the correlation between the large-scale turbulence in boundary layer and flow distributions around the urban obstacles, we believe the impact of the atmospheric motions transmitted by the canopy flow around the building on the wall pressure, which is the driving force of wind-induced natural ventilation.

In this context, we have conducted simultaneous outdoor measurements of the flow within and above the canopy layer and the wall pressure acting on a scale model within square arrays in order to understand their mutual relations. In this paper, we discuss the sensitivity of wall pressure to the unsteady atmospheric flow conditions (such as the wind speed, direction, and turbulence) and try to identify the relative importance of the flow above and within the canopy layer to account for the temporal and spatial variations of the wall pressure.

## 2. Experimental methodology

### 2.1. Details of measurement field site

Outdoor measurements were conducted at the Comprehensive Outdoor Scale Model experiment site (COSMO) at the Nippon Institute of Technology in Saitama, Japan ( $39^{\circ}04'$  north latitude,  $139^{\circ}07'$  east longitude). Fig. 1(a) is a schematic view of the COSMO site. It consists of  $32 \times 16 (= 512)$  building models regularly aligned in a square array with a packing density,  $\lambda_p$ , of 25% on a  $100 \text{ m} \times 50 \text{ m}$  concrete foundation. The height of cubical models,  $H$ , is 1.5 m which is approximately 1/5 of the height of typical residential buildings such as 2-storied detached houses. The ratio of  $H$  to the street width,  $W$ , is 1.0. The longitudinal direction of the site is set along the prevailing wind direction during summer and winter (i.e., northwestern (NW) and southeastern (SE) directions). Further details of COSMO facility are provided by Kanda et al. [22].

During the period of our measurements, from 24th to January 27, 2018, NW was observed as the predominant wind direction. Hence, as illustrated in Fig. 1(b), the streamwise velocity,  $u$ , is defined as the velocity of the NW wind along the longitudinal direction of the site, and  $v$  and  $w$  are the spanwise and vertical wind velocities, respectively. The corresponding axes are defined as  $x$ ,  $y$  and  $z$ , respectively. Accordingly, the wind direction  $\theta$ , which is the angle between chord of  $x$  axis and the velocity vector in the horizontal plane, is ranging from  $-180$  to  $180$  as shown in Fig. 1(b) (i.e., the opposite direction from the meteorological definition). The wind directions are sequentially labeled from Angle 01 to Angle 12 with a separation of  $30$  between each, as depicted in Fig. 1(c). For example, the wind direction parallel with the  $x$  axis with  $-15^{\circ} < \theta \leq 15^{\circ}$  is defined as Angle 06.

During the measurement period, other field experiments were simultaneously conducted in one part of the COSMO site. Specifically, it should be noted that a sun shade, called “Fractal Sun Shade”, with a size

**Table 1**

List of the sonic anemometers. The positions (x, y, z) for each anemometer are defined with respect to the red cross position shown in Fig. 2(b) and (c).

Name	Sonic anemometer		Accuracy [ $^{\circ}$ C]	Accuracy [m/s]	Sampling [Hz]	Location		
	Vender	Probe				x	y	z
A1	Young	CYG-81000	$\pm 2$	$\pm 0.05$	10	$2.5H$	$0.5H$	$1.5H$
A2						$2.5H$	$0.5H$	$2H$
L	Kaijo	TR-90AH	—	$\pm 0.005$		$1.1H$	$0.5H$	$0.5H$
W				$\pm 0.005$		$1.9H$	$0.5H$	$0.5H$

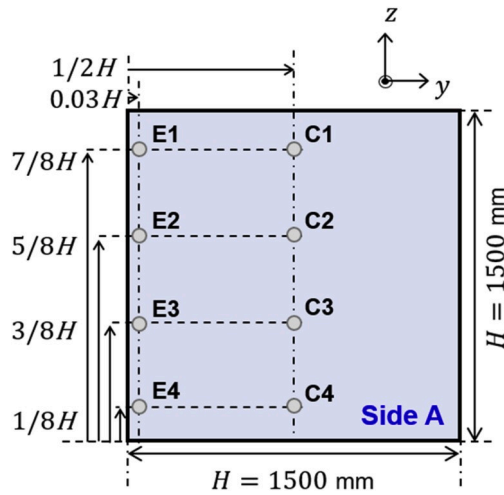


Fig. 3. Positions of pressure taps on side A of the target block.

of 20 m  $\times$  20 m, was installed 1.1 m above the block height at the SE half, as represented by the grey square in Fig. 1(a). Thus, the location of target block for the present measurements was carefully selected as the position where there are sufficiently long separation distance from the sun shade, which is 11 columns and 5 rows from the northern corner of the site.

As for the scaling effect of the building models in COSMO site, since the ratio of convective boundary layer height  $\delta$  against the building height  $H$  must be smaller than that in WTEs and  $H$  itself is small compared to the realistic building scale, the experiments in COSMO site cannot be compared either WTEs or full-scale field measurements. On the other hand, the internal boundary layer height  $\delta_i$ , which means that the boundary layer adjusted by the underlying block arrays, might have the depth comparable with that of WTEs because of the limited fetch length ( $20H$  for the present target block) as revealed by Cheng and Castro [23]. Since our measurements were conducted under the flow fields which was well influenced by the block arrays, the canopy flow and internal boundary layer flow can be comparable with those observed in WTEs. Furthermore, COSMO site allows us to measure the velocity field affected by the atmospheric flow, which cannot be reproduce in WTEs. Therefore, we regard the present measurement as a valuable study to fill the gaps between WTEs and full-scale measurements.

## 2.2. Experimental set-up for wind speed and wall pressure

Fig. 2(a) is a photograph taken from the western side, showing the target block and the measurement apparatus installation. To observe flow field conditions, we set up the four sonic anemometers listed in Table 1. As illustrated in Fig. 2(b), two sonic anemometer-thermometers were placed at  $0.5H$  and  $1H$  above the top of the target block (hereafter, A1 and A2 respectively). Inside the canopy, two sonic anemometers were installed nearby, along the leeward and windward walls at  $0.5H$  height (hereafter, L and W, respectively). All the sonic anemometers

were located at the spanwise center of the target block, as depicted in Fig. 2(c). The three velocity components  $u$ ,  $v$ , and  $w$  (also referred to as  $u_i$  with  $i = 1, 2, 3$ ), were recorded at the sampling frequency of 10 Hz by all the sonic anemometers. Temperature data were recorded by A1 and A2.

In addition to the sonic anemometers, 10 mm-thick acrylic plates with pressure taps of 3.2 mm-diameter holes were installed on both the NW and SE sides of the target block, labeled as side A and side B in Fig. 2 (b), respectively. The plates were attached using 40 mm-wide aluminum frames screwed onto the cubical target block. Therefore, the actual length of the target block in the streamwise direction was 1.6 m (frame width: 0.04 m, acrylic plate thickness: 0.01 m for both sides, and the total thickness of the frame and plate: 0.1 m), whereas the block height was 1.5 m. Aluminum tubes of 20 mm length were inserted into each hole on the acrylic plate and were connected to silicon tubes. The outside faces of the acrylic plate and aluminum tubes were carefully adjusted to be identical. The void spaces created between the plates and the block faces were used to install the silicon tubes connected to the taps. The tubes were gathered together and connected to pressure manometers (OKANO, DPC-500N12, error on pressure  $p \pm 0.1$  Pa), which were placed in a container located next to the target block (Fig. 2(c)). The dimensions of the container were approximately  $0.7 \times 0.4 \times 0.6$  m<sup>3</sup>. Although the container could have slightly affected the air flow between the blocks, it was necessary to position it there to avoid response delay of the pressure manometers, which depended on the length of the tubes between the pressure taps and the sensors. Fig. 3 illustrates the detailed positions where the wall pressure was measured. Positions C1–C4 and E1–E4 were located at the center (C) and near-edge (E) lines of the block face, respectively. Each pressure manometer measured the pressure differences between block faces on side A and side B at each position with a sampling frequency of 10 Hz. The pressure differences denoted as  $\Delta p = p_A - p_B$  were simultaneously measured at eight different locations on the block faces using eight manometers. Both the pressure and velocity were continuously collected using a data logger (GRAPHTECH, GL7000) with a frequency of 10 Hz. Except for the pressure manometers, all devices were placed in containers located  $2H$  away from the target block as shown in Fig. 2 (c).

## 3. Measurement conditions

### 3.1. Wind directions of the approaching flow

Atmospheric flow has strong variations of wind speeds and directions, which characterizes the background conditions of the approaching flow in the current outdoor measurements. To determine the variation of such flow, we illustrated the wind rose diagram for the instantaneous horizontal wind speed at  $z = 1.5H$  as  $u_h = (u_{1.5H}^2 + v_{1.5H}^2)^{0.5}$  [m/s] for the entire measurement period in Fig. 4. Here, the roughness sublayer is assumed to be above the height of  $1.5H$  in COSMO site, according to the experimental data by Inagaki and Kanda [24]. Applying the classification in wind angles defined in Fig. 1(c) to the instantaneous horizontal wind direction at  $z = 1.5H$ ,  $\theta_h$ , the sampling numbers of each event and the mean wind speed at each angle are shown in Fig. 4(a) and (b), respectively. When  $u_h < 1.0$ , the wind speed distribution was uniformly observed in each direction whereas the



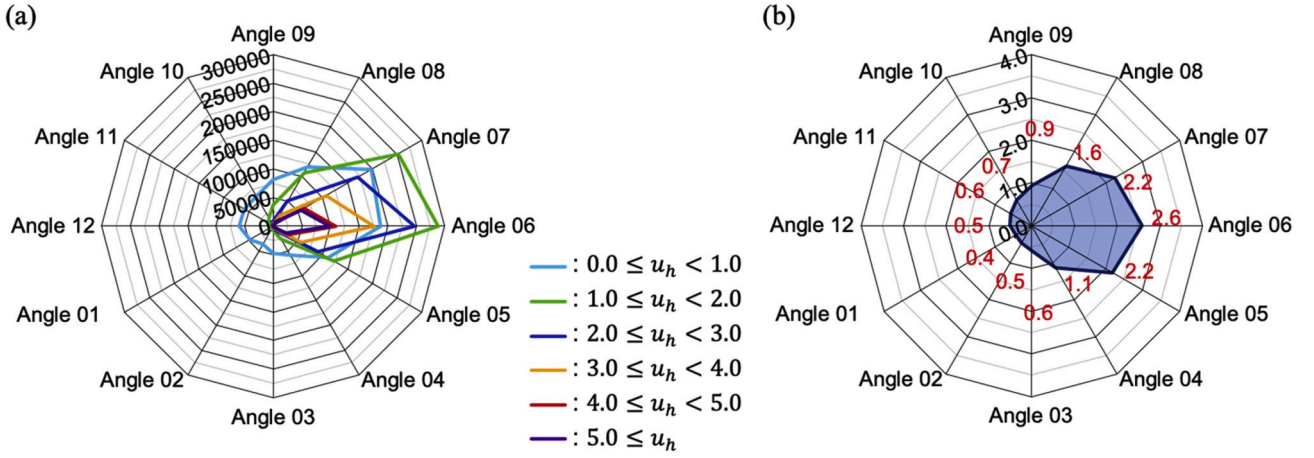


Fig. 4. Wind rose diagram for the instantaneous horizontal wind speed obtained at height  $1.5H$ . (a) Sampling number classified by wind speed,  $u_h$  [m/s], and flow angle,  $\theta_h$  [°]. (b) Mean wind speed for each angle,  $\theta_h$  [°]. Wind direction,  $\theta_h$ , defined as Angles 01 to 12.

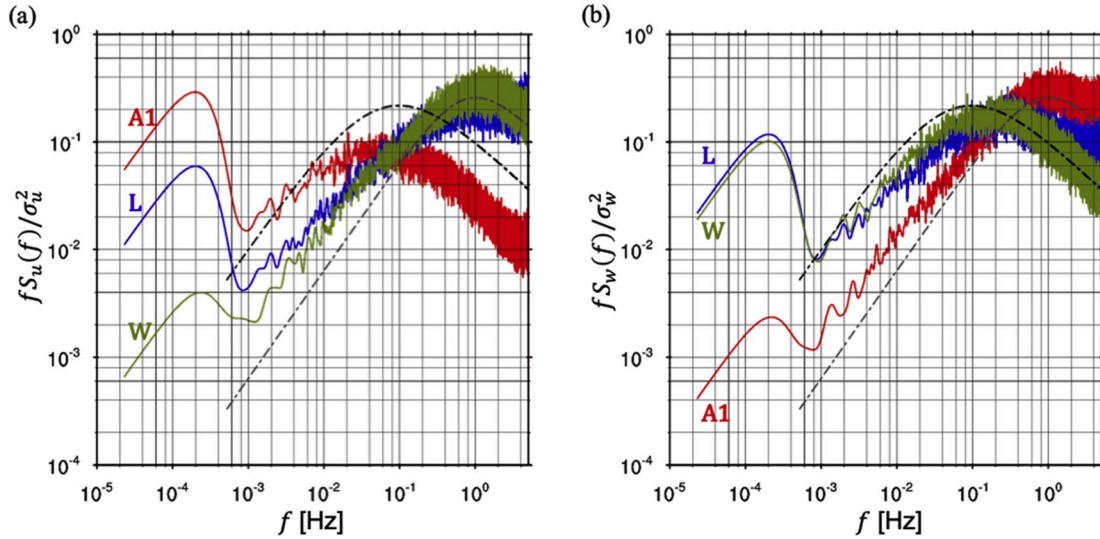


Fig. 5. Power spectral density  $fS_{u_i}/\sigma_{u_i}$  of (a) streamwise and (b) vertical velocity obtained at A1, L and W. Black and grey dashed-dotted lines indicate spectral density of streamwise and vertical velocity components by Kaimal et al. [25], respectively. Both axes are logarithmic.

dominant flow directions in Fig. 4(a) were Angle 06 and Angle 07 (i.e., NW wind) when  $u_h \geq 1.0$ . The mean wind speed categorized into Angle 06 had the largest value compared to the other angles (Fig. 4(b)). Therefore, the aerodynamic effect of the sun shade located in SE side of the target block (in Fig. 1(a)) is negligible (, as it was proven by the previous measurement in COSMO site by Hirose et al. [19]).

### 3.2. Spectral density

To understand the composition of atmospheric flow with large-scale eddies and to justify the present data averaging period of 10 min, we calculated the spectral density for the velocity and pressure differences by means of the fast Fourier transform. The power spectra density  $S_x(f)$  is expressed by Eqs. (3)–(1).

$$S_x(f) = \frac{1}{T} \{X(f)X^*(f)\}, \quad (3-1)$$

where  $X(f)$  is the Fourier transform of the time-series data  $x(t)$  with period  $T$  [s] calculated by the fast Fourier transform and  $X(f)^*$  denotes the complex conjugate of  $X(f)$ .

The power spectral densities of  $u$  and  $w$  at A1, L and W on January

26, 2018 are shown in Fig. 5. In addition, the spectra densities by Kaimal et al. [25] are also provided in Fig. 5. The spectral densities are formulated as,

$$S_u(f) = 105\alpha_u^2 a (1 + 33af)^{-\frac{5}{3}}, \quad (3-2)$$

$$S_w(f) = 2\alpha_w^2 a \left(1 + 5.3a^{\frac{5}{3}}f^{\frac{5}{3}}\right)^{-1}, \quad (3-3)$$

where  $\alpha_{u_i} = V^*/\sigma_{u_i}$ ,  $V^*$  [m/s] is the friction velocity,  $\sigma_{u_i}$  [m/s] is the standard deviation of the velocity component  $u_i$ ,  $a = (z - d)/V$ ,  $z (= 1.5H)$  is the measurement height at A1,  $d (= 0.87H)$  [m] is the displacement height [24], and  $V$  [m/s] is the mean streamwise velocity.  $V$ ,  $V^*$ , and  $\sigma_{u_i}$  are calculated based on the data during  $T$ . In Fig. 5, the spectral densities are scaled by  $\sigma_{u_i}^2$ .

In the high frequency region, the spectral density obtained at A1 in Fig. 5(a) shows good agreement with Eqs. (3)–(2) in terms of the peak frequency of  $f \sim 1 \times 10^{-1}$  Hz and the theoretical slope of  $-\frac{2}{3}$ . In contrast, the peak frequency of the spectral densities at L and W occurred at the frequency of  $f \sim 2$  Hz, which are higher than that at A1. Interestingly,

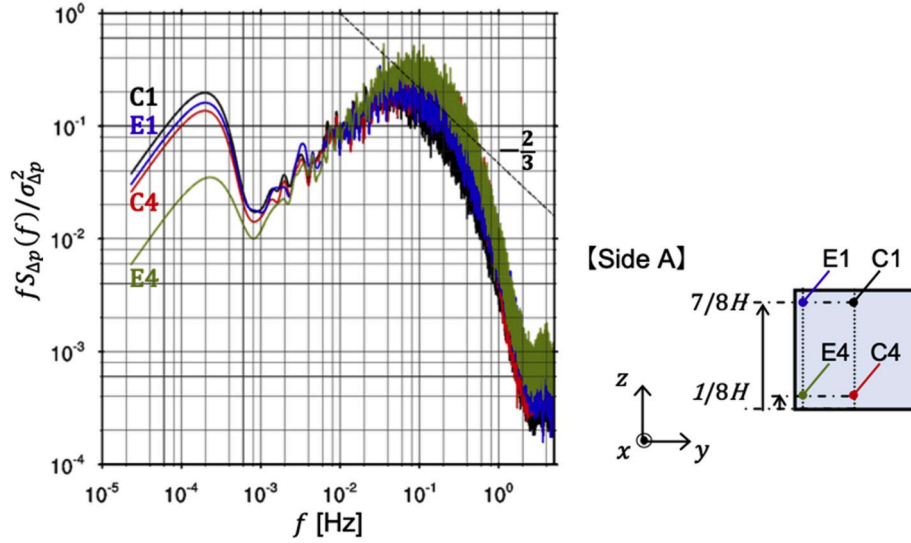


**Fig. 6.** Power spectral density of wall pressure difference  $fS_{\Delta p}(f)/\sigma_{\Delta p}^2$  obtained at measurement positions, C1, E1 (at  $z = 7/8H$ ), C4 and E4 (at  $z = 1/8H$ ).  $\sigma_{\Delta p}$  represents standard deviation of  $\Delta p$  during total period,  $S_{\Delta p}$ . Dash line have a slope of  $-2/3$ . Both axes are logarithmic.

**Table 2**

Atmospheric conditions measured at height,  $2H$ . Wind speed,  $u_h$  [m/s]; Reynolds number,  $Re$ ; roughness Reynolds number,  $Re^*$ ; stability parameter,  $\xi$ , were calculated with selected data based on the data-screening criteria.

	$u_h$ [m/s]	$Re$	$Re^*$	$\xi$
Selected data	3.00 ( $\pm 0.05$ )	$3.2 \times 10^5$	$4.6 \times 10^3$	0.0031

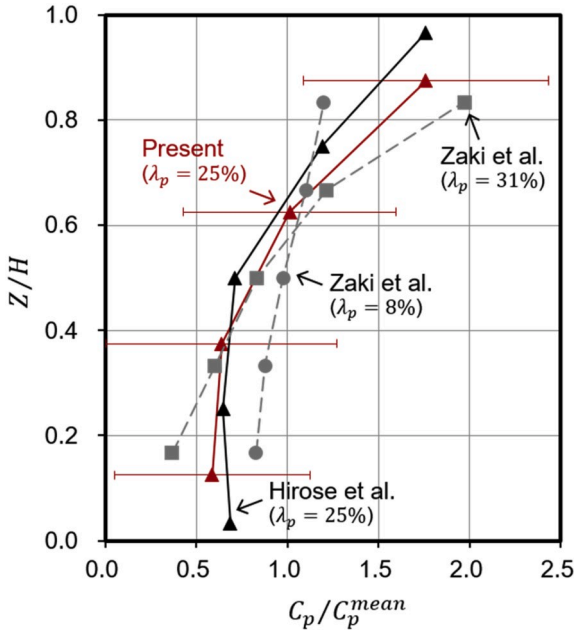


**Fig. 7.** Vertical distribution of  $C_p/C_p^{mean}$ . The grey colored circles and squares are the results, reported by Zaki et al. [31], of WTEs for cubical square arrays with a packing density of 8% and 31%, respectively. The black triangles represent the results, reported by Hirose et al. [19], of field measurements.  $C_p^{mean}$  denotes the area average of  $C_p$  over the block face ( $C_p^{mean} = 1/H^2 \int C_p dydz$ ) and error bars represent the standard deviation,  $\sigma_{C_p}$ , of  $C_p$  determined each 10 min.

the peaks at L and W well correspond to that in Eqs. (3)–(3), indicating that the turbulence characteristics of the streamwise velocity component within the canopy are caused by those of the vertical component above the canopy. This might be because the flow above the canopy changed into the flow along the leeward and windward walls in the canopy, resulting in the shift of the spectral peak frequency at W and L from that of A1. Furthermore, at the lower frequency region in Fig. 5(a), the spectral peak is around  $f \sim 2 - 3 \times 10^{-4}$  Hz. Since this frequency corresponds to a duration  $t \sim 1.4 - 0.9$  h, this peak is due to large-scale atmospheric turbulence. It is noteworthy that these spectral peak values tend to be small at L and W, indicating the turbulence generated by the block arrays is dominant within the canopy even though large scale fluctuation of atmospheric turbulence exists above the canopy.

The power spectral densities of the vertical velocity component in Fig. 5(b) show the spectral peaks of L and W at around  $f \sim 2 - 3 \times 10^{-4}$  Hz, whereas the peak is considerably weak at A1. In addition, the other spectral peaks of  $S_w(f)$  can be seen at  $f \sim 2 \times 10^{-1}$  Hz for L and W. In contrast, the peak of  $S_w(f)$  of A1 occurred at  $f \sim 1 - 2$  Hz. These results indicate that the peak frequencies in the high frequency regions of  $S_w$  approximately correspond to Eqs. (3)–(2) at L and W and Eqs. (3)–(3) at A1, respectively. These facts imply that the vertical flow along the leeward and windward walls are strongly affected by the turbulence characteristics of the streamwise velocity component above the canopy.

In addition, the power spectral densities of  $\Delta p$  on January 26, 2018 are shown in Fig. 6, which indicate the contribution of various eddies on the pressure fluctuation. In the low frequency region,  $S_{\Delta p}(f)$  has almost similar tendency as  $S_u(f)$  at A1. Specifically, a clear spectral gap around  $f \sim 10^{-3}$  Hz with a secondary peak for  $S_{\Delta p}(f)$  at  $f \sim 2 - 3 \times 10^{-4}$  Hz is observed. The values of the secondary peak are smaller than the dominant peaks near  $f \sim 10^{-1}$  Hz, whereas those of  $S_u(f)$  at A1 show comparable values. In addition, the secondary peak of  $S_{\Delta p}(f)$  is distinct, whereas the peak of  $S_u(f)$  at W is apparently weak. In contrast, the rates of the spectral decay are obviously higher than  $-2/3$  in the high frequency area. It is noteworthy that this discrepancy between the spectral densities of the velocity and wall pressure was also observed in the WTE and full-scale measurement by Kawai et al. [26]. Hunt et al. [27] theoretically explained that such discrepancies of the spectral decay are caused by the distortion of the turbulence in the immediate vicinity of the windward face, which reduces the turbulent fluctuation of the wall pressure especially in the higher frequency domain.

To separate the effects of the large- and small-scale turbulences observed in the spectral densities, averaging in shorter periods than the

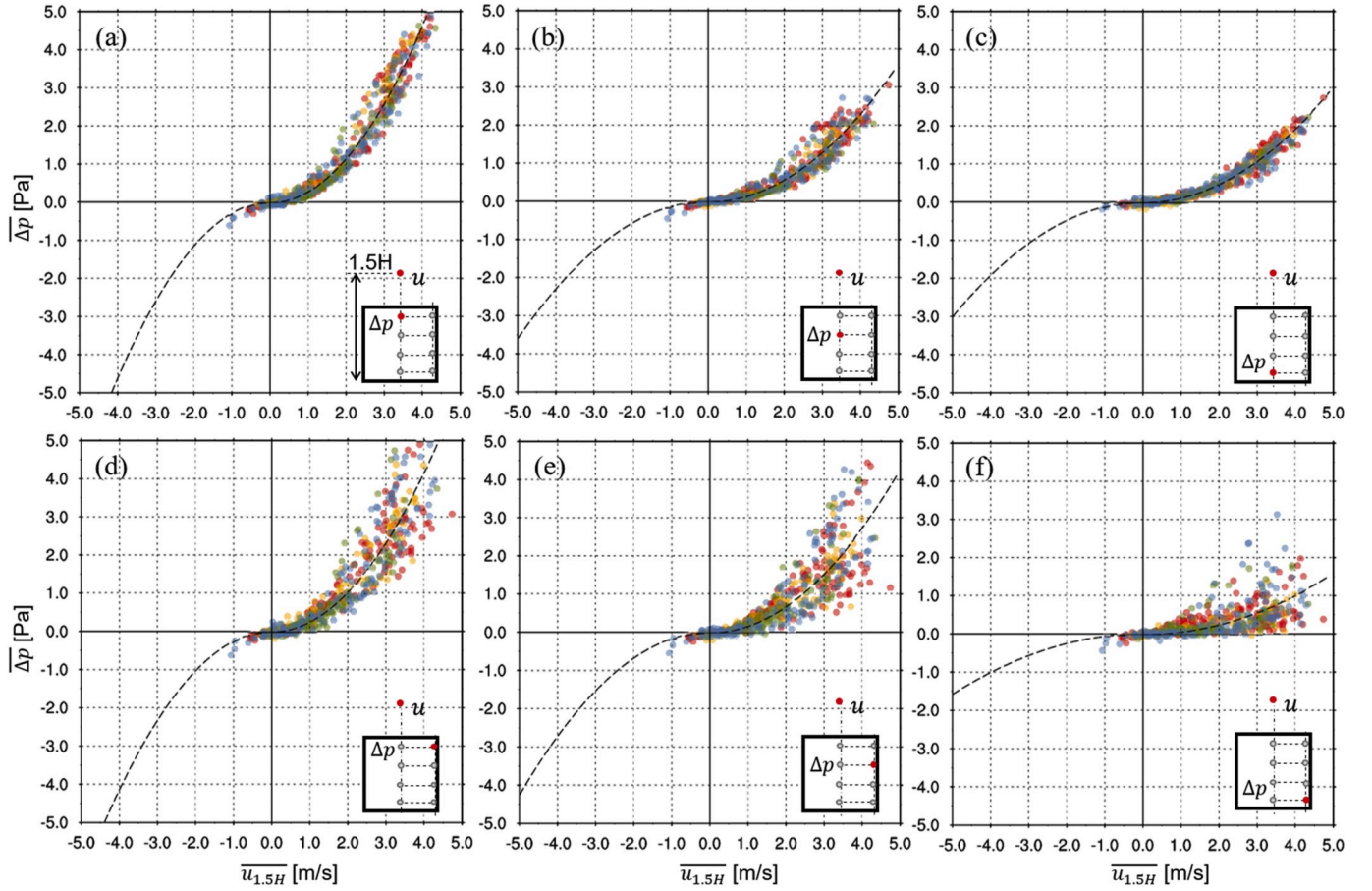


Fig. 8. Relationship between wall pressure difference  $\overline{\Delta p}$  and streamwise velocity  $\overline{u}_{1.5H}$  measured at different dates and positions: (a) C1, (b) C2, (c) C4, (d) E1, (e) E2, and (f) E4. The dashed lines show  $\overline{\Delta p} = 0.5\rho\overline{u}_{1.5H}^2C_p$ , where  $C_p$  is the deduced pressure coefficient.

spectrum gap is commonly used [24]. The spectral gaps were clearly observed near  $f \sim 10^{-3}$  Hz in our measurements (Figs. 5 and 6), which is consistent with current knowledge on the spectral gaps, found between 10 min and 30 min [28]. Therefore, 10 min, which is a shorter period than this gap, was chosen as the averaging period for both  $u_i$  and  $\Delta p$ .

### 3.3. Data selection

Some data were eliminated based on measurement errors of the wall pressure and the stratification of the boundary layer according to the following two criteria. The first criterion is  $|\overline{u}_{2H}| \geq 1.0$  m/s, where  $\overline{u}_{2H}$  represents the averaged streamwise velocity component at  $z = 2H$  because of the measurement accuracy of the manometers ( $\pm 0.1$  Pa). Hereafter,  $\overline{\varphi}$  is equal to the 10-min average, and  $\varphi' = \varphi - \overline{\varphi}$  represents its deviation for any value of  $\varphi$ . The subscript,  $2H$  or  $1.5H$ , represents the value measured at  $z = 2H$  or  $1.5H$ , respectively. When  $|\overline{u}_{2H}| \sim 1.0$ ,  $\Delta p = 0.5\rho\overline{u}_{2H}^2C_p \sim 0.10 - 0.17$  Pa ( $C_p \sim 0.24 - 0.41$  from the present results and [19]), which is comparable with the limits of accuracy of the manometer. The second criterion is  $-0.05 < \xi < 0.05$ , following Inagaki and Kanda [24], since we focused on neutral conditions, where  $\xi$  is the non-dimensional parameter for the stability defined by the following equation at  $z = 2H$ .

$$\xi = \frac{z'}{L} = -\frac{\kappa z' g w' T'}{\overline{T} u'^3} \quad (3-4)$$

Here,  $L$  [m] is the Obukhov length,  $z' = z - d$  [m] is the effective height defined by the difference between  $z$  and displacement height,  $d$  [m] ( $= 0.87H$ ) [24],  $\kappa$  ( $= 0.4$ ) is the von Karman constant,  $g$  [ $\text{m/s}^2$ ] is gravitational acceleration,  $w'T'$  [ $\text{K}\cdot\text{m/s}$ ] is the turbulent heat flux,  $\overline{T}$  is

the potential temperature [K], and  $u^*$  [m/s] is the friction velocity estimated by the shear stress as  $u^{*2} = \sqrt{(\overline{u'w'})^2 + (\overline{v'w'})^2}$  [28].

Flow statistics of the selected data are summarized in Table 2. In Table 2, all the variables are defined at height,  $2H$ . The Reynolds number for the selected data is  $Re = u_i H / \nu \approx 3.2 \times 10^5$ , where  $\nu$  [ $\text{m}^2/\text{s}$ ] is the kinematic viscosity. In addition, the estimated roughness Reynolds number  $Re^* = u^* z_o / \nu$  determined by roughness length,  $z_o$ , was larger than  $O(1)$  based on the assumption,  $z_o = 0.1H$ , where  $O$  is the Landau symbol [29]. Therefore, the fully rough conditions, where turbulent flow within and near the canopy satisfies the scale similarity, were achieved [30] owing to the large scale of the outdoor experiment compared to those of WTEs. Therefore, the abovementioned results enabled a comparison between the outdoor experimental data in this study and previous experimental data, such as Zaki et al. [31] or computational scale model results, such as Coceal et al. [32], conducted in the neutral stratification.

### 3.4. Pressure coefficient

The wind pressure coefficient,  $C_p$ , was determined by a least squares method of all selected data using Eqs. (3)–(5):

$$\overline{\Delta p} = 0.5\rho\overline{u}_{1.5H}^2C_p, \quad (3-5)$$

where  $\overline{u}_{1.5H}$  represents the averaged streamwise velocity component at  $z = 1.5H$ .

Fig. 7 shows a comparison of the vertical variations of  $C_p/C_p^{\text{mean}}$  with the measurement data observed at the COSMO site with various wind directions by Hirose et al. [19] (black triangles) and the WTE data under



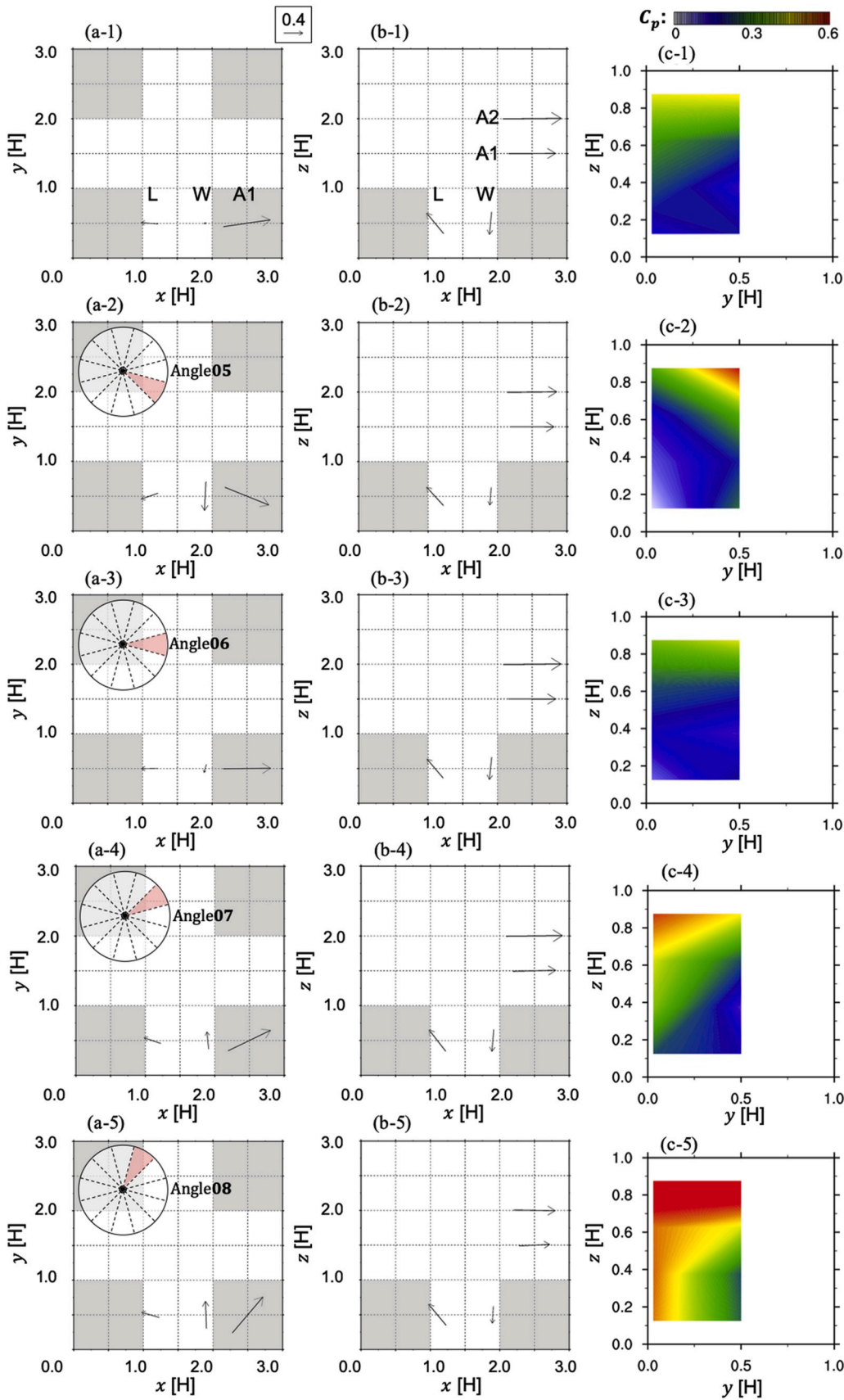


**Fig. 9.** Distributions of the mean flow and pressure coefficient. Velocity vectors in (a) horizontal and (b) southeastern-side views. The velocity observed by each anemometer was normalized by the wind speed at A1 according to:  $U_{1.5H} = \{\overline{u_{1.5H}^2} + \overline{v_{1.5H}^2}\}^{0.5}$  or  $U_{1.5H}^N = \{(\overline{u_{1.5H}^N})^2 + (\overline{v_{1.5H}^N})^2\}^{0.5}$ . (c) Distributions of  $C_p$ . (1) represents  $\langle \overline{\varphi} \rangle$ , while (2)–(5) show  $\overline{\varphi}^N$  for  $N = \text{Angle05, 06, 07 and 08, respectively}$ . The origin of the coordinate system in the figures are consistent with the reference position in Fig. 2(b) and 2(c). (For interpretation of the references to color in this figure legend, the reader is referred to the Web version of this article.)



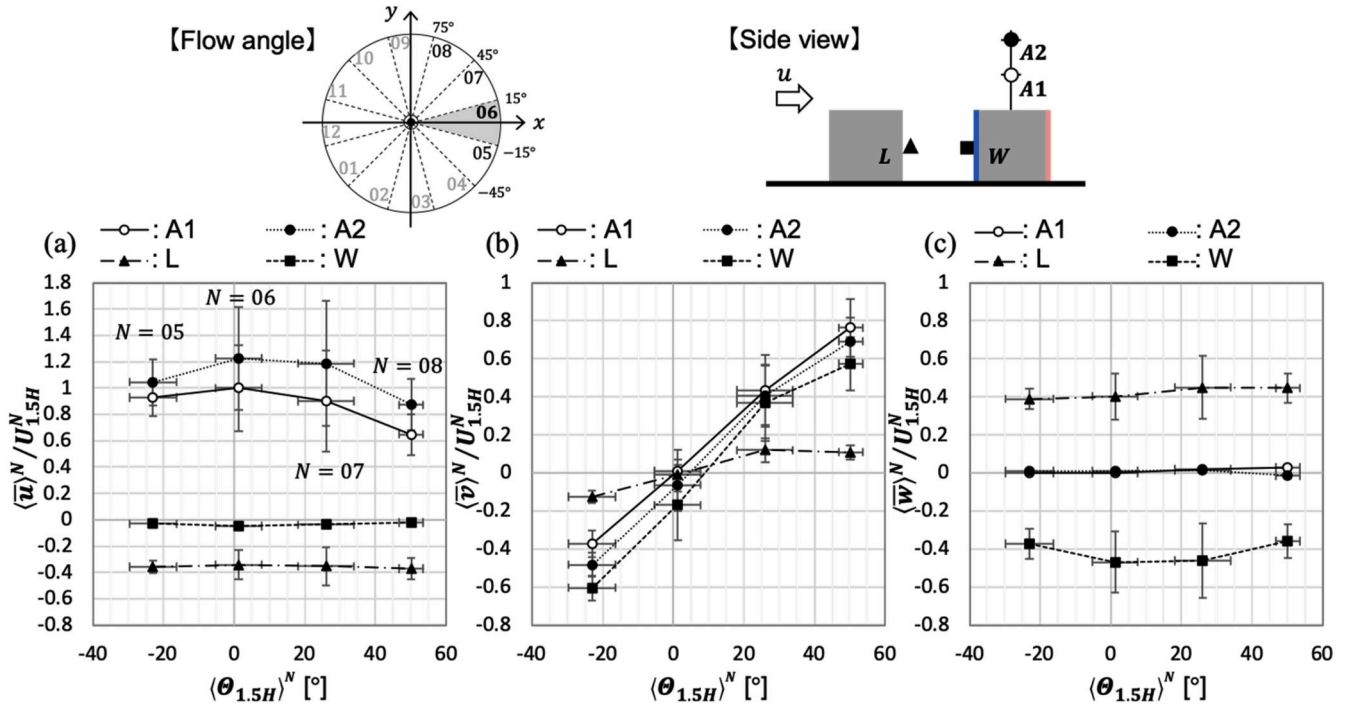


**Fig. 10.** Mean velocity,  $\bar{u}_i^N$ , within and above the canopy as a function of the mean reference wind direction,  $\Theta_{1.5H}^N$ . Wind speed was scaled by  $U_{1.5H}^N = (\{\bar{u}_{1.5H}^N\}^2 + \{\bar{v}_{1.5H}^N\}^2)^{0.5}$  and the error bars in the vertical and horizontal axes represent the standard deviation of  $\bar{u}_i^N$  and  $\Theta_{1.5H}^N$  ( $\sigma_{u_i}^N$  and  $\sigma_{\Theta_{1.5H}}^N$ ), respectively.

the conditions of the square arrangement and the wind orthogonal to cubic models obtained by Zaki et al. [31] (grey circles ( $\lambda_p = 8\%$ ) and squares ( $\lambda_p = 31\%$ )), where  $C_p^{mean}$  indicates spatially-averaged  $C_p$  over the block surface ( $C_p^{mean} = 1/H^2 \int C_p dy dz$ ). The present result is reasonably consistent with those from the WTEs because its profile has intermediate values between them. In addition, the present data is consistent with that of field measurements by Hirose et al. [19]. It is remarkable that the qualitative characteristics in the profiles of  $C_p$  do not change, even though the present results are inevitably affected by the fluctuation of the approaching wind speed, wind direction and turbulent scales in the atmospheric boundary layer.

Fig. 8 show the relationships between the approaching wind speed,  $\bar{u}_{1.5H}$ , and wall pressure,  $\bar{\Delta p}$ , on the target block.  $C_p$ , derived from  $\bar{u}_{1.5H}$  and  $\bar{\Delta p}$  by the least squares method, are also depicted with dashed lines in Fig. 8(a). Fig. 8(a) and (d) show that an increase of  $\bar{u}_{1.5H}$  yields the more significant increment of  $\bar{\Delta p}$  at the highest measurement positions compared to those at the other heights. This is because the high-speed flow above the canopy can easily impinge on the top end line of the block. Moreover, the values of  $\bar{\Delta p}$  for the near-edge line (Fig. 8(d) to 8(f)) are more scattered than those for the center line (Fig. 8(a) to 8(c)). In addition, this tendency is enhanced with increasing values of  $\bar{u}_{1.5H}$ . Furthermore, the gradient of the best-fit curves of  $C_p$  tends to increase with the measurement height and the deviations of  $\bar{\Delta p}$  from the regressed lines become larger at the near-edge line than at the center line. This means that  $C_p$  may vary probably owing to large scale variation. Such effect is more significant on the near-edge line than that on the center line.

#### 4. Effect of wind direction on mean flow and pressure

##### 4.1. Distributions of mean flow and wall pressure

To examine the main features in the flow and pressure fields, we compared the distributions of the mean flow around the target block and

wall pressure acting on it. The mean of the temporal averaged values is calculated according to Eqs. (4)–(1).

$$\bar{\varphi} = \frac{1}{M} \sum_M \bar{\varphi}, \quad (4-1)$$

where  $M$  ( $=382$ ) denotes the total number of the temporally-averaged quantities  $\bar{\varphi}$  extracted by criteria in 3.3. The mean wind vectors in the horizontal and vertical sections are shown in Fig. 9(a-1) and 9(b-1), respectively. The horizontal view includes velocity vectors at both  $z = 0.5H$  and  $1.5H$ . The velocity vector is normalized by the temporally averaged wind speed at A1, according to:  $U_{1.5H} = \{\bar{u}_{1.5H}^2 + \bar{v}_{1.5H}^2\}^{0.5}$ . Figs. 9(c-1) illustrates the distribution of  $\langle C_p \rangle$ . The origins of the coordinate in the figures are consistent with the red cross position in Fig. 2 (b) and 2 (c). From Figs. 9(a-1) and 9(b-1), we can confirm that the well-known cavity flow pattern consisting of downward and upward flows along the windward and leeward walls was dominant during the measurement period because of the prevailing wind orthogonal to the block face.  $\langle C_p \rangle$  is affected by the stable structure of the cavity flow, and Figs. 9(c-1) shows a typical distribution with large values on the top end line of the block, which is often reported by various CFD studies of regular block arrays, such as Coceal et al. [32] and Claus et al. [33]. For further analysis of the mutual relationships between the flow and pressure fields, the conditional average depending on the mean wind angle  $\Theta_{1.5H}$  was examined. Here,  $\Theta_{1.5H}$  is defined according to Fig. 1. (c) based on  $\bar{u}_{1.5H}$  and  $\bar{v}_{1.5H}$ . The conditional average of  $\bar{\varphi}$  is described as  $\bar{\varphi}^N$  when  $\Theta_{1.5H}$  is in Angle  $N$ .

$$\bar{\varphi}^N = \frac{1}{M} \sum_M \bar{\varphi} \text{ when } \Theta_{1.5H} \text{ in Angle } N. \quad (4-2)$$

Here,  $M$  represents the sample numbers for each angle.  $M$  is 16, 240, 108, 18 for Angle 05, 06, 07 and 08, respectively.

The obtained results are shown in Figs. 9(a-2) to 9(c-5). The velocity vector was normalized by the conditionally averaged wind speed at A1 denoted as  $U_{1.5H}^N = \{\bar{u}_{1.5H}^{N2} + \bar{v}_{1.5H}^{N2}\}^{0.5}$ .  $\Theta_{1.5H}$  corresponds to the

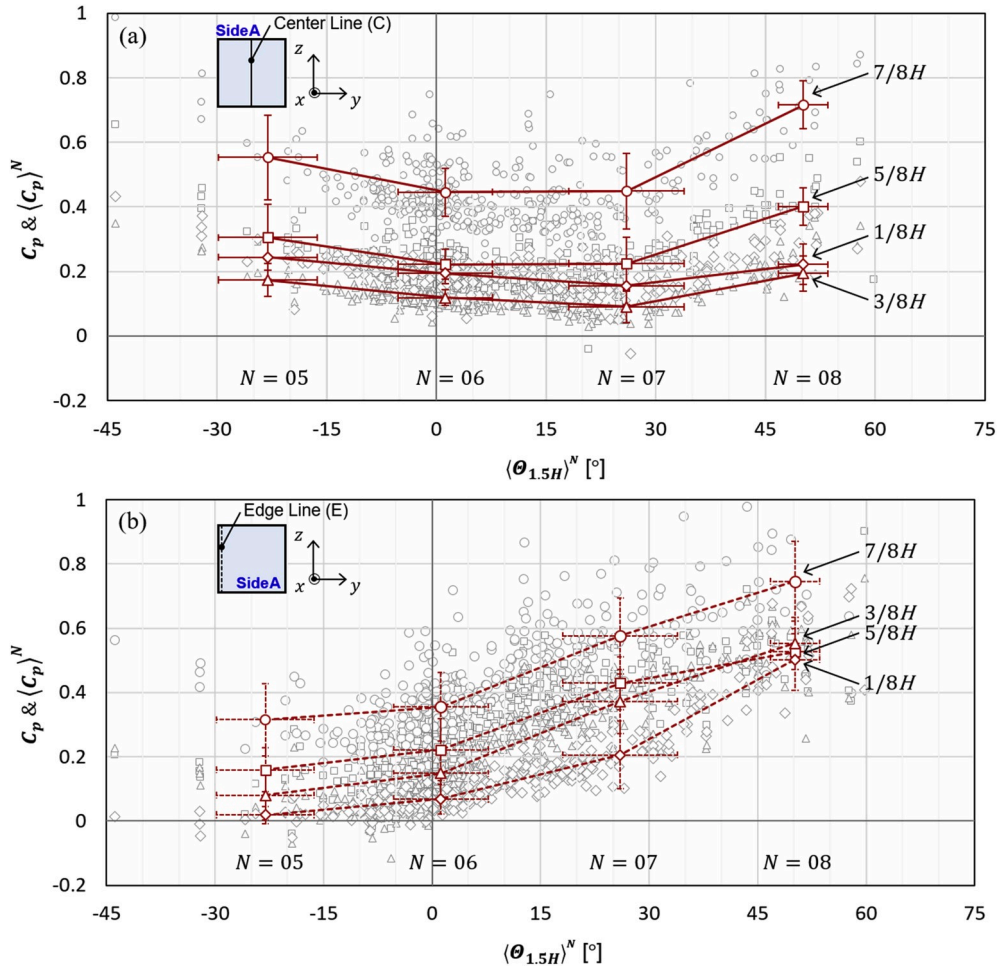


**Fig. 11.** Dependence of pressure coefficient,  $C_p$  and  $C_p^N$  on the reference wind direction,  $\theta_{1.5H}$  at the (a) center line (C), and (b) near-edge line (E). The error bars in the vertical and horizontal axes represent the standard deviation of  $C_p$  and  $\theta_{1.5H}$  ( $\sigma_{C_p}^N$  and  $\sigma_{\theta_{1.5H}}^N$ ), respectively. The symbols represent different measurement heights, z. circle: 7/8H, rectangular: 5/8H, triangle: 3/8H, and rhombus: 1/8H.

horizontal angle of the arrows at A1 in Figs. 9(a-2) to 9(a-5). Furthermore, the similar flow patterns near the walls to those in Fig. 9(1-b) are observed in Figs. 9(b-2) to 9(b-5), even though the approaching flow has different values of  $\theta_{1.5H}$ . In contrast,  $\theta_{1.5H}$  clearly changes  $C_p^N$  in Figs. 9(c-2) to 9(c-5). Comparing Figs. 9(c-2) and 9(c-4), the largest pressure points due to the impingement of the approaching flow on the windward face move to the side where the approaching flow originates when  $\theta_{1.5H} / = 0$ . The values of  $C_p^{07}$  become larger than  $C_p^{06}$  even near the lowest height (Figs. 9(c-4)). These results clearly indicate that flow direction dramatically changes  $C_p$  distributions even though similar flow structures such as the upward flow at L and the downward flow at W are generated regardless of  $\theta_{1.5H}$ .

The spanwise wind direction at W in Angle 05 (Figs. 9(a-2)) and Angle 07 (Figs. 9(a-4)) suggest deep entrainment of the inclined approaching wind in the cavity between the two blocks from the street. The wind direction within the cavity was more parallel with the windward face of the blocks than the inclined approaching flow. In contrast, the canopy flow at L was less affected by a change in  $\theta_{1.5H}$ .

#### 4.2. Relationship between pressure coefficient and wind speeds within and above canopy

We analyzed the dependence of  $\bar{u}_i$  and  $C_p$  on  $\theta_{1.5H}$  to investigate the considerable temporal and spatial variations in the wall pressure due to the wind direction of the approaching flow.

Fig. 10 shows the conditional averaged wind speed,  $\bar{u}_i^N$ , scaled by the wind speed at A1,  $U_{1.5H}^N$ , with respect to the approaching wind direction in Angle N. The horizontal axis represents the mean wind direction,  $\theta_{1.5H}$  and the error bars in each axis show the standard deviation of the conditional averaged data,  $\sigma_{\bar{u}_i^N}^N$ , depending on  $\theta_{1.5H}$  defined by the following equation.

$$\sigma_{\bar{u}_i^N}^2 = \frac{1}{M} \sum_M (\bar{u}_i - \bar{u}_i^N)^2 \text{ when } \theta_{1.5H} \text{ is in Angle } N. \quad (4-3)$$

In Fig. 10(a),  $\bar{u}^N$  at A1 and A2 have their maximum values in Angle 06 and gradually decreases with the inclination of the reference wind direction. In contrast,  $\bar{u}^N$  at L and W are almost constant with  $\theta_{1.5H}^N$ . Because of the entrainment of high-speed flow above the canopy into the cavity resulting in the distinct downward flow at W shown in Fig. 9(b),  $\bar{u}^N$  at W is nearly zero while  $\bar{u}^N$  at L is negative, or reverse flow. In contrast, as shown in Fig. 10(b),  $\bar{v}^N$  at W is enhanced with an increase of  $\theta_{1.5H}^N$ . This tendency is also observed at A1 and A2. Furthermore,  $\bar{v}^N$  at L slightly increases with  $\theta_{1.5H}^N$  because its measurement position is located within the wake of the upstream block.  $\bar{w}^N$  at A1 and A2 in Fig. 10(c) exhibits general characteristics of the boundary-layer flow, specifically smaller wind speed in the vertical component compared with the horizontal component. However, within the canopy,  $\bar{w}^N$  at L and W become considerably positive and negative values, respectively, because neighboring building walls cause downdraft and updraft along the walls. In addition, the strength of such updraft and downdraft is insensitive to the

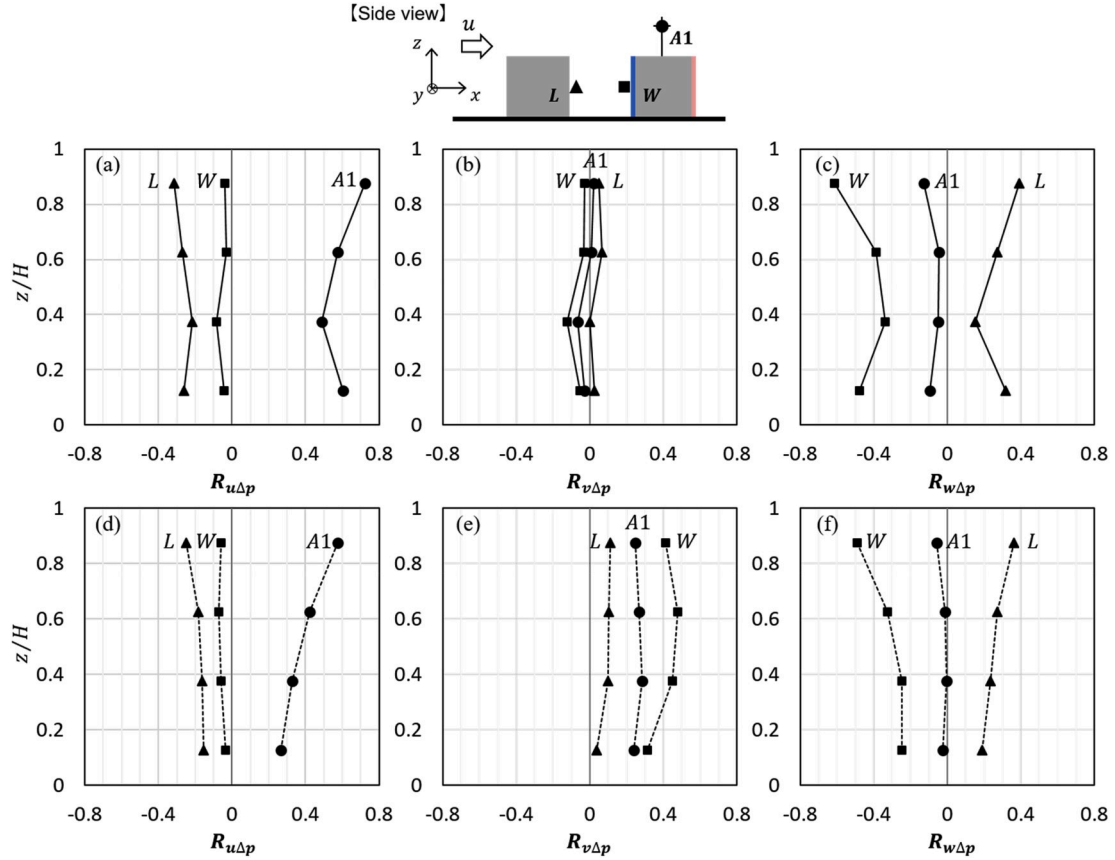


**Fig. 12.** Vertical profiles of two-point correlation coefficient,  $R_{u\Delta p}$ . Streamwise (a, d), spanwise (b, e), and vertical (c, f) velocities. Wall pressure difference,  $\Delta p$ , at the center (a, b, c) and near-edge (d, e, f) lines. Measurement positions for velocity are shown in the schematic side view above the plots.

reference wind direction. These tendencies of  $\bar{u}^N$  and  $\bar{w}^N$  indicate that robust cavity circulation can be formed regardless of the wind direction under the current building configuration, as apparent in the vector maps in Fig. 9.

Fig. 11 shows the sensitivity of  $C_p$  and  $C_p^N$  to  $\theta_{1.5H}^N$ .  $C_p^N$  at  $z = 7/8H$  and  $5/8H$  in Fig. 11(a) show relatively small values when the wind direction is  $\theta_{1.5H} \sim 0$  and tend to become larger with an increase of  $\theta_{1.5H}$ . For example, the value of  $C_p^{08}$  in Angle 08 is 1.6 times greater than that in Angle 06 at  $z = 7/8H$ . In contrast,  $C_p^N$  at  $z = 3/8H$  and  $1/8H$  in Fig. 11(a) seem to be almost independent of  $\theta_{1.5H}^N$ . This is consistent with the fact that the cavity flow pattern at the vertical center line is insensitive to  $\theta_{1.5H}^N$  as confirmed in Section 4.1. Furthermore, all  $C_p^N$  at the near-edge line increase with  $\theta_{1.5H}^N$ . The values of  $C_p^{08}$  at  $z = 7/8H$  and  $z = 1/8H$  shown in Fig. 11(b) are 2.1 and 7.4 times larger than  $C_p^{06}$ , respectively. Therefore, we can conclude that the sensitivity of  $C_p$  to  $\theta_{1.5H}$  is much stronger at the near-edge line than at the center line on the block surface, especially in the lower-height area of the building surface. In addition, the distribution of  $C_p$  is more sensitive to  $\theta_{1.5H}$  than the velocity distribution within the canopy.

## 5. Statistical relationships between velocity and pressure fields

### 5.1. Correlation coefficient between velocity and pressure

The two-point correlation coefficient,  $R_{u\Delta p}$ , was calculated according to Eqs. (5)–(1).

$$R_{u\Delta p} = \frac{\int_T u_i'' \Delta p'' dt}{\left( \int_T u_i''^2 dt \int_T \Delta p''^2 dt \right)^{0.5}} \quad (5-1)$$

Here,  $u_i'' = u_i - \frac{1}{T} \int_T u_i dt$  and  $\Delta p'' = \Delta p - \frac{1}{T} \int_T \Delta p dt$  indicate the deviation part of  $u_i$  and  $\Delta p$  from the temporal average of the measurement period extracted by criteria in Section 3.3,  $T$ . The deviations of  $u''$  and  $\Delta p''$  are defined by the difference between the instantaneous values and average during  $T$  to clarify the correlation between velocity and pressure differences due to both the large- and small-scale variations. Fig. 12 shows the vertical profiles of  $R_{u\Delta p}$  at the center and near-edge lines of the target block.

At the center line, shown in Fig. 12(a),  $R_{u\Delta p}$  at A1 shows the stronger correlation compared with those at L and W. In particular,  $R_{u\Delta p}$  at A1 is 0.60, even at  $z = 1/8H$ , indicating that the pressure fluctuation at the lower center point on the block face was affected by the perturbation of the approaching wind speed above the canopy. In contrast,  $R_{u\Delta p}$  at L and W show only weak negative or no correlation because of the robust upward and downward flow at L and W, respectively, as shown in Fig. 10. (c) as well as Fig. 9. (b-1). Furthermore,  $R_{u\Delta p}$  at L is higher than that at W, while L is located at the center on the leeward wall of upstream block of the target block where  $\Delta p$  is measured. This might be because  $\Delta p$  tends to fluctuate due to high-speed, downward flow at W which can also generate the reverse flow at L in the cavity as mentioned in Section 4.2. This speculated flow pattern is also consistent with the result of the strong negative correlation of  $R_{w\Delta p}$  at W in Fig. 12(c).  $R_{u\Delta p}$  and  $R_{w\Delta p}$  at the near-edge line shown in Fig. 12(d) and (f) have similar tendencies to those at the center line. These results indicate that both the flow above the canopy and the resulting cavity flow (such as the downward flow at windward wall and the upward flow at leeward wall) have significant effects on the wall pressure fluctuations at both the center and near-edge lines on the block.

A different trend for  $R_{v\Delta p}$  at center and near-edge lines was observed as shown in Fig. 12(b) and (e). The positive values of  $R_{v\Delta p}$  in Fig. 12(e)

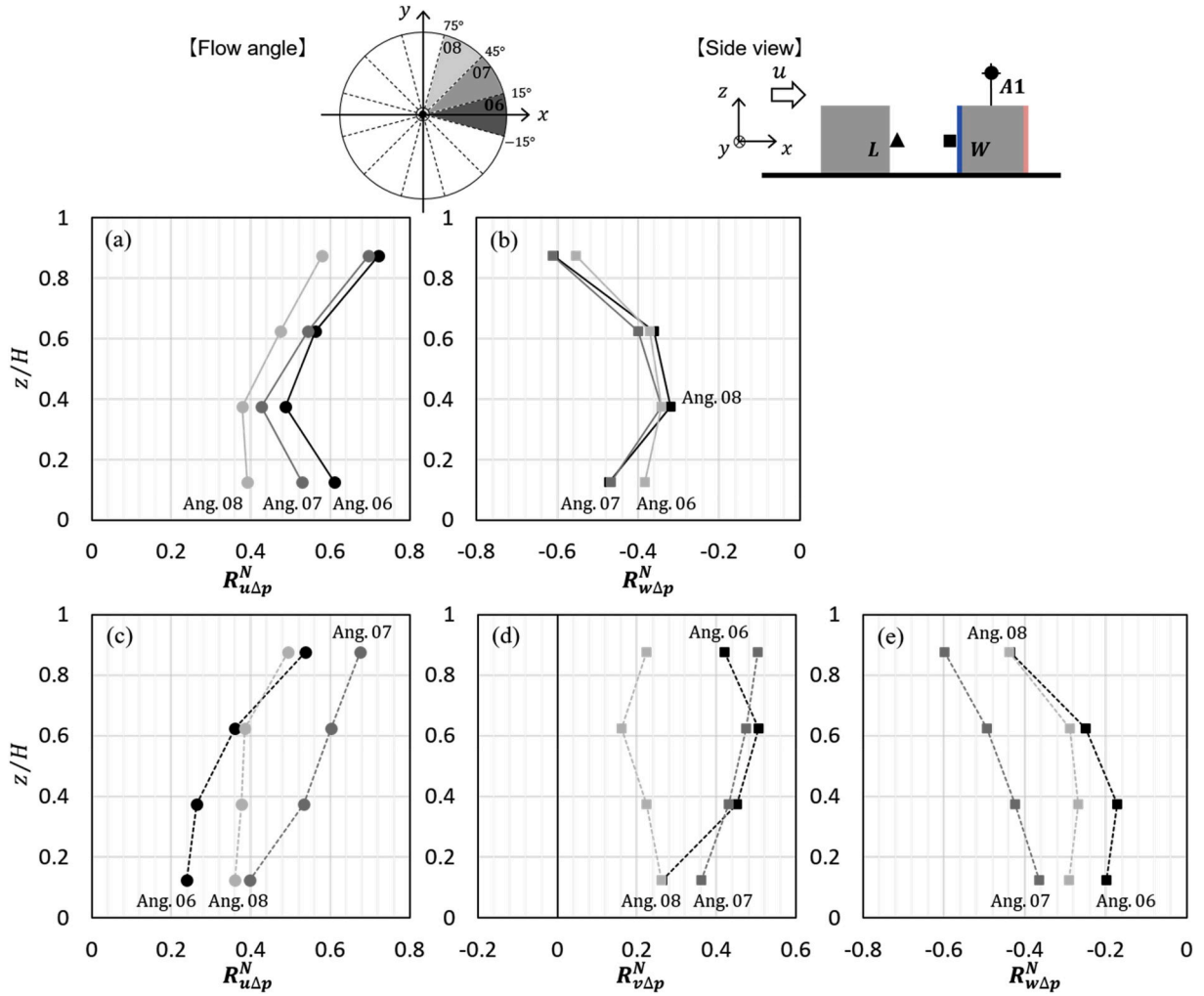


Fig. 13. Two-point correlation coefficient,  $R_{u\Delta p}^N$ , calculated by: wall pressure difference,  $\Delta p$ , at the center line and (a) streamwise velocity at A1 or (b) vertical velocity at W; wall pressure difference,  $\Delta p$ , at near-edge line and (c) streamwise velocity at A1, (d) spanwise velocity at W, or (e) vertical velocity at W. The black, grey, and light grey lines represent the flow directions of Angle 06, 07, and 08, respectively.

suggest that the acceleration (deceleration) of  $v$  especially at W and somewhat at A1 can enhance (decrease)  $\Delta p$  on the side-edge line of the block surface due to the strong entrainment of the airflow from the street, which is absent in the center line (Fig. 12(b)).

In summary, the temporal changes in  $\Delta p$  on the center line of the block surface are caused by fluctuations of  $u$  at A1 and  $w$  at W, while those at the near-edge line are also accounted for by fluctuations of  $v$  at W. The strong correlation between  $\Delta p$  and  $w$  at W might be explained by sustained fluctuations of  $w$  within canopy by the strong downwind flow along the windward wall, from  $u$  above the canopy. Furthermore,  $\Delta p$  strongly correlated with the airflow above the canopy, suggesting that fluctuations in wall pressure and the resultant indoor ventilation within the canopy layer is strongly affected by turbulent flow above the canopy and is less sensitive to the turbulence generated within the canopy.

## 5.2. Effect of approaching wind direction

The two-point correlation coefficient,  $R_{u\Delta p}^N$ , was calculated according to Eqs. (5)–(2).

$$R_{u\Delta p}^N = \frac{\int_T u_i'' \Delta p'' dt}{\left( \int_T u_i''^2 dt \int_T \Delta p''^2 dt \right)^{0.5}} \text{ when } \Theta_{1.5H} \text{ is in Angle } N. \quad (5-2)$$

The profiles of  $R_{u\Delta p}^N$  on the center and near-edge lines are shown in Fig. 13. In Fig. 13(a),  $R_{u\Delta p}^{06}$  shows the largest positive correlation on the

center line and  $R_{u\Delta p}^N$  slightly decreases with increasing  $\Theta_{1.5H}$ . However,  $R_{u\Delta p}^N$ , which represents the fluctuation of  $u$  at A1, makes a contribution to the wall pressure on the center line irrespective of  $\Theta_{1.5H}$ , even in the lowest case. In contrast,  $R_{u\Delta p}^{06}$  and  $R_{u\Delta p}^{08}$  on the near-edge line (Fig. 13(c)) show a weaker positive correlation compared to  $R_{u\Delta p}^{07}$ . The vertical average of  $R_{u\Delta p}^{07}$  on the near-edge line is 0.55, and is 1.6 times larger than that of  $R_{u\Delta p}^{06}$ . These results suggest that the flow introduced into the canopy layer impinges effectively on the near-edge line of the block wall when the approaching flow is inclined to some extent, whereas this impingement is weaker when the wind direction is sufficiently large, such as Angle 08.

At the near-edge line, shown in Fig. 13(d),  $R_{v\Delta p}^{06}$  and  $R_{v\Delta p}^{07}$  have stronger positive correlations than  $R_{v\Delta p}^{08}$ . This is because the efficient introduction of the approaching flow above the canopy at Angle 07 causes the flow to impinge on the side-edge of the block surface (i.e.,  $\Delta p' > 0$ ) and generate acceleration of the spanwise flow at W (i.e.,  $v' > 0$ ). As a result, positive  $R_{v\Delta p}^{07}$  slightly decreases with height. In contrast,  $R_{v\Delta p}^{06}$  shows positive correlations comparable to  $R_{v\Delta p}^{07}$  at  $z = 3/8H$  and  $5/8H$  because the flow parallel to the street increases the streamwise flow, resulting in entrainment of high-speed flow from the street even at the lower canopy height. These trends support the fact that  $R_{v\Delta p}^{08}$  becomes very low due to weak impingement on the wall and weak



airflow along the street.

In Fig. 13(b), no differences in  $R_{w\Delta p}^N$  at the center line due to  $\theta_{1.5H}$  are observed, consistent with flow impinging on the block and causing vertically downward flow along the block face (as shown in Figs. 9(b) and Fig. 10(c)). In contrast,  $R_{w\Delta p}^N$  at the near-edge line in Fig. 13(e) shows weak correlation in Angle 06 and strong correlation in Angle 07. In the case of Angle 07, the introduction of high-speed flow above the canopy can cause both downward and horizontal spanwise flow at W which have the dominant contribution to pressure fluctuation at the near-edge line. In contrast, in the case of Angle 06, pressure distribution at the near-edge line is due to entrainment of the accelerated flow from the street into the cavity which generates only horizontal spanwise flow at W.

In summary, wall pressure fluctuation is more sensitive to the approaching flow at the side-edge than at the center line of the block, suggesting that the dominant factor varying wall pressure arises from different flow patterns.

## 6. Conclusion

We conducted simultaneous outdoor measurements of the roughness sublayer flow and wall pressure differences between the windward and leeward faces on the cubic scale model within the square arrays at the COSMO site. Making use of the advantage of the outdoor field measurements, we evaluated the impact of the approaching flow under realistic atmospheric conditions in terms of wind speed, direction, and turbulence.

The following results were mainly obtained in this study. Firstly, the discrepancy between  $C_p$  averaged for 10 min and  $C_p$  deduced by the least squares method revealed that  $C_p$  values might change spatially and temporally owing to realistic atmospheric flow conditions. Because the discrepancy was pronounced at the side-edge of the block surface under the current geometric condition, the estimation of the ventilation potential might be inaccurate by means of the conventional approach. Secondly, both of the downward and upward flows along the windward and leeward walls were observed as the mean flow structure. This flow fields were insensitive to the approaching flow direction. In contrast, the distributions of  $C_p$  were apparently affected by the approaching wind direction. Thirdly, the correlation coefficient,  $R_{u\Delta p}$ , indicated that the entrainment of high-speed flow from above the canopy and from the street considerably influenced the fluctuation of wall pressure under the current geometric conditions. These results imply that the fluctuation of the wall pressure difference and resultant indoor ventilation could be affected by the turbulent flow above the canopy.

On the other hand, the aforementioned results cannot be generalized in other geometric conditions. This is because they cause the significant changes in canopy flow patterns affected by the atmospheric turbulent flow above the canopy layer. Therefore, we intend to study the aforementioned contributions of the flow around the buildings to the wall pressure in detail under various geometric conditions in future work.

## Declaration of competing interest

The authors declare that they have no known competing financial interests or personal relationships that could have appeared to influence the work reported in this paper.

## Acknowledgement

The authors are grateful to Ms. C. Yamashita and Mr. R. Hikizu for their assistance with the outdoor measurements. This work was supported by JSPS KAKENHI grants (JP17H04946, JP17KK0117).

## References

- [1] R. Buccolieri, M. Sandberg, H. Wigö, S. Di Sabatino, The drag force distribution within regular arrays of cubes and its relation to cross ventilation – theoretical and experimental analyses, *J. Wind Eng. Ind. Aerod.* 189 (2019) 91–103.
- [2] Y. Tominaga, B. Blocken, Wind tunnel experiments on cross-ventilation flow of a generic building with contaminant dispersion in unsheltered and sheltered conditions, *Build. Environ.* 92 (2015) 452–461.
- [3] L. Ji, H. Tan, S. Kato, Z. Bu, T. Takahashi, Wind tunnel investigation on influence of fluctuating wind direction on cross natural ventilation, *Build. Environ.* 46 (2011) 2490–2499.
- [4] M. Shirzadi, Y. Tominaga, P.A. Mirzaei, Wind tunnel experiments on cross-ventilation flow of a generic sheltered building in urban areas, *Build. Environ.* 158 (2019) 60–72.
- [5] O.S. Asfour, M.B. Gadi, A comparison between CFD and Network models for predicting wind-driven ventilation in buildings, *Build. Environ.* 42 (2007) 4079–4085.
- [6] G. Evola, V. Popov, Computational analysis of wind driven natural ventilation in buildings, *Energy Build.* 38 (2006) 491–501.
- [7] R. Ramponi, B. Blocken, CFD simulation of cross-ventilation for a generic isolated building: impact of computational parameters, *Build. Environ.* 53 (2012) 34–48.
- [8] S. Murakami, Overview of turbulence models applied in CWE — 1997, *J. Wind Eng. Ind. Aerod.* 76 (1998) 7–22.
- [9] Y. Tominaga, Flow around a high-rise building using steady and unsteady RANS CFD: effect of large-scale fluctuations on the velocity statistics, *J. Wind Eng. Ind. Aerod.* 142 (2015) 93–103.
- [10] J. Seifert, Y. Li, J. Axley, M. Rösler, Calculation of wind-driven cross ventilation in buildings with large openings, *J. Wind Eng. Ind. Aerod.* 94 (2006) 925–947.
- [11] Y. Tominaga, T. Stathopoulos, Numerical simulation of dispersion around an isolated cubic building: model evaluation of RANS and LES, *Build. Environ.* 45 (2010) 2231–2239.
- [12] N. Ikegaya, C. Hirose, A. Hagishima, J. Tanimoto, Effect of turbulent flow on wall pressure coefficients of block arrays within urban boundary layer, *Build. Environ.* 100 (2016) 28–39.
- [13] Y. Jiang, Q. Chen, Study of natural ventilation in buildings by large eddy simulation, *J. Wind Eng. Ind. Aerod.* 89 (2001) 1155–1178.
- [14] H. Wang, Q. Chen, A new empirical model for predicting single-sided, wind-driven natural ventilation in buildings, *Energy Build.* 54 (2012) 386–394.
- [15] A. Inagaki, M. Kanda, Organized structure of active turbulence over an array of cubes within the logarithmic layer of atmospheric flow, *Boundary-Layer Meteorol.* 135 (2010) 209–228.
- [16] L.J. Lo, A. Novoselac, Cross ventilation with small openings: measurements in a multi-zone test building, *Build. Environ.* 57 (2012) 377–386.
- [17] H. Gough, T. Sato, C. Halios, C.S.B. Grimmond, Z. Luo, J.F. Barlow, A. Robertson, R. Hoxey, A. Quinn, Effects of variability of local winds on cross ventilation for a simplified building within a full-scale asymmetric array: overview of the Silsoe field campaign, *J. Wind Eng. Ind. Aerod.* 175 (2018) 408–418.
- [18] H. Gough, M.F. King, P. Nathan, C.S.B. Grimmond, A. Robins, C.J. Noakes, Z. Luo, J.F. Barlow, Influence of neighbouring structures on building façade pressures: comparison between full-scale, wind-tunnel, CFD and practitioner guidelines, *J. Wind Eng. Ind. Aerod.* 189 (2019) 22–33.
- [19] C. Hirose, N. Ikegaya, A. Hagishima, J. Tanimoto, Outdoor measurement of wall pressure on cubical scale model affected by atmospheric turbulent flow, *Build. Environ.* 160 (2019) 106–170.
- [20] M. Kanda, Large-eddy simulations on the effects of surface geometry of building arrays on turbulent organized structures, *Boundary-Layer Meteorol.* 118 (2006) 151–168.
- [21] H. Takimoto, A. Sato, J.F. Barlow, R. Moriwaki, A. Inagaki, S. Onomura, M. Kanda, Particle image velocimetry measurements of turbulent flow within outdoor and indoor urban scale models and flushing motions in urban canopy layers, *Boundary-Layer Meteorol.* 140 (2011) 295–314.
- [22] M. Kanda, M. Kanega, T. Kawai, R. Moriwaki, H. Sugawara, Roughness lengths for momentum and heat derived from outdoor urban scale models, *J. Appl. Meteorol. Climatol.* 46 (2007) 1067–1079.
- [23] H. Cheng, Ian P. Castro, Near-wall flow development after a step change in surface roughness, *Boundary-Layer Meteorol.* 105 (2002) 411–432.
- [24] A. Inagaki, M. Kanda, Turbulent flow similarity over an array of cubes in near-neutrally stratified atmospheric flow, *J. Fluid Mech.* 615 (2008) 101–120.

- [25] J.C. Kaimal, J.C. Wyngaard, Y. Izumi, O.R. Cote, Spectral characteristics of surface-layer turbulence, *Quart. J.R. Met. Soc.* 98 (1972) 563–589.
- [26] H. Kawai, J. Katsura, H. Ishizaki, Characteristics of pressure fluctuations on the windward wall of a tall building, *Wind Eng.* 1 (1980) 519–528.
- [27] J.C.R. Hunt, H. Kawai, S.R. Ramsey, G. Pedrizetti, R.J. Perkins, A review of velocity and pressure fluctuations in turbulent flows around bluff bodies, *J. Wind Eng. Ind. Aerod.* 35 (1990) 49–85.
- [28] R.B. Stull, *An Introduction to Boundary Layer Meteorology*, Kluwer Academic Publishers, 1988.
- [29] R.W. MacDonald, R.F. Griffiths, D.J. Hall, An improved method for the estimation of surface roughness of obstacle arrays, *Atmos. Environ.* 32 (1998) 1857–1864.
- [30] W.H. Snyder, I.P. Castro, The critical Reynolds number for rough-wall boundary layers, *J. Wind Eng. Ind. Aerod.* 90 (2002) 41–54.
- [31] S.A. Zaki, H. Hagishima, J. Tanimoto, Experimental study of wind-induced ventilation in urban building of cube arrays with various layouts, *J. Wind Eng. Ind. Aerod.* 103 (2012) 31–40.
- [32] C. Coceal, T.G. Thomas, I.P. Castro, S.E. Belcher, Mean flow and turbulence statistics over groups of urban-like cubical obstacles, *Bound.-Layer Meteorol.* 121 (2006) 491–519.
- [33] J. Claus, O.C.T. Glyn, S.B.S.E. Belcher, I.P. Castro, Wind-direction effects on urban-type flows, *bound. -Layer Meteorol* 142 (2012) 265–287.